Radioimmunotherapy with radioactive nanoparticles: First results of dosimetry for vascularized and necrosed solid tumors

V. Bouchat,[a] V. E. Nuttens, and S. Lucas
Laboratoire d'Analyses par Réactions Nucléaires (LARN), University of Namur (FUNDP), Rue de Bruxelles 61, B-5000 Namur, Belgium

C. Michiels
Unité de Recherche en Biologie Cellulaire (URBC), University of Namur (FUNDP), Rue de Bruxelles 61, B-5000 Namur, Belgium

B. Masereel
Department of Pharmacy (DP), University of Namur (FUNDP), Rue de Bruxelles 61, B-5000 Namur, Belgium

O. Féron
Unité de Pharmacothérapie (FATH), Université Catholique de Louvain (UCL), Avenue Mounier, 53, B-1200 Brussels, Belgium

B. Gallez
Laboratoire de resonance magnétique biomédicale (CMFA), Université Catholique de Louvain (UCL), Avenue Mounier, 73, B-1200 Brussels, Belgium

T. Vander Borght
Center for Molecular Imaging and Experimental Radiotherapy (IRME), Université Catholique de Louvain (UCL), Dr. G. Therasse, 1, B-5530 Yvoir, Belgium

(Received 29 June 2007; revised 7 September 2007; accepted for publication 7 September 2007; published 29 October 2007)

Radioimmunotherapy uses monoclonal antibodies that are still labeled with only one radioactive atom. The aim of this paper is to assess, by means of MCNPX simulations, the doses delivered around and throughout a solid tumor when the radioactive atom linked to each antibody is replaced by a 5 nm diameter nanoparticle composed of numerous radionuclides. A new model for a spherical vascularized tumor has been developed in which the antibody distributions inside the tumor can be uniform or heterogeneous. It is also possible to simulate a central necrotic core inside the tumor where the concentration of radiolabeled antibodies is assumed to be zero. Dosimetry calculations have been performed for the beta-emitting radionuclide $^{90}Y_2O_3$. Preliminary results show that the irregularity of vasculature and the presence of a necrotic core have a noticeable influence on the deposited dose profiles. Moreover, with a total activity of 5 and 34 MBq for tumor radii of 0.5 and 1.0 cm, respectively, viable tumor cells can receive doses of up to 50 Gy, even if high nonuniformity of the total activity is observed in the tumor. These simulations still require accurate information about antibody characteristics and necrosis sizes but clearly confirm that the use of monoclonal antibodies conjugated to nanoparticles could lead to a considerable enhancement of treatment efficacy against cancer.
[DOI: 10.1118/1.2791038]

Key words: radioimmunotherapy, dosimetry, Monte Carlo, tumor model, nanomedicine

I. INTRODUCTION

In radioimmunotherapy (RIT), radionuclides coupled to monoclonal antibodies (mAb's) are increasingly used to deliver ionizing radiation to kill tumor cells while sparing normal tissue.[1–3] The radiolabeled antibodies are directed against various antigens overexpressed on tumor cells or blood vessels formed during angiogenesis.[4–6] Each time, only one radioactive atom is linked to the antibody and the delivered tumor doses in RIT are influenced mainly by the antibody properties, the choice of radionuclide, and the biological halflife of the complex.[1,7] This approach for treating cancer shows good results for hematopoietic malignancies such as non-Hodgkin's lymphoma, which require only low doses of radiation ($\sim$15 Gy).[8–12] Unfortunately, clinical studies have shown that solid tumors are less sensitive to ionizing radiation and doses higher than 60 Gy are necessary to observe therapeutic effects.[7] New strategies to increase antibody accumulation and penetration into the tumor are currently being investigated but the delivered doses remain insufficient to observe an important treatment response.[13–16] Today, it is possible to assemble several nonradioactive metal atoms to form clusters of nanometer dimensions.[17–20] Hence, we have conceptually designed a nanoparticle composed only of radioactive elements to enhance diagnostic sensitivity in medical imaging or to improve therapeutic effectiveness in RIT.

A major obstacle in the use of nanoparticulate systems for drug delivery is the process of opsonization responsible for a rapid clearance of these clusters from circulation by the reticuloendothelial system (RES), comprising mainly the Kupffer Cells in the liver as well as spleen and bone marrow macrophages.[21–24] Nevertheless, progress in nanomedicine has shown that the behavior and stability of a nanoparticle within the biological microenvironment can be controlled by its size and surface characteristics. For example, large macromolecules ($\geqslant$100 nm) move slowly in tissue, and this has the effect of enhancing their clearance by the host defense RES.[25] By creating spherical radioactive nanoparticles whose diameter does not exceed 5 nm, the radiolabeled complex is small enough to reduce its uptake by the RES hence promoting its diffusion through the target tissue. The surface of these nanoparticles can also be covered by nonionic surfactants or polymeric macromolecules to form a protective layer against the absorption of opsonin proteins required for macrophage recognition. For example, coating nanoparticles with polyethylene glycol (PEG) or PEG-containing copolymers increases their blood halflife after intravenous administration.[22,24–27] These long hydrophilic polymer chains located on the surface of the particles have the advantage of reducing interparticulate attractive van der Waals forces and preventing the aggregation of several nanoclusters. Finally, the polymeric coating of the nanoparticle can be functionalized with targeting molecules such as the antibodies, therapeutic drugs, or image contrast agents to create a multifunctional nanoparticle.[21,28,29]

Nanoparticles have already been investigated in medicine and have demonstrated promising application for tumor targeting.[29,30] For example, quantum dots (QDs), nanosized fluorescent semiconductor particles, are rapidly becoming an interesting tool for detecting tumors[31] and therapeutic treatments could be considered by simply adding drugs around these QDs.[32–34] Magnetic[28,35,36] or metal[37–39] nanoparticles coupled to antibodies are also in development for quality improvement of magnetic and optical imaging. Functionalized with additive ligands, these nanoparticles could offer new opportunities for treating cancer. The advantages of using radioactive nanoparticles in RIT are threefold. First, even if half of the atoms encapsulated in the nanoparticle are no longer radioactive when the antibodies reach the tumor, the activity delivered by a nanoparticle is higher than the activity given by a single radioactive atom. Hence, antibodies conjugated to nanoparticles should deliver higher radiation dose to the tumors. Potential cluster radiolysis should however, be studied. Second, different types of radionuclides can be combined (α, β, γ, or x-ray emitters) or mixed with nonradioactive atoms used in medicine such as magnetic elements. Third, nanoparticles have more surface area to accommodate a large number of different types of functional groups so that more than one antibody can be conjugated.

As the energy deposition of such radioactive nanoparticles is unknown, dosimetry simulations are required to calculate the absorbed doses inside and around the tumor and to establish the best therapeutic treatment for the patient. An approach using Monte Carlo N-Particles eXtended Software (MCNPX) to determine the radiation dose absorbed by tumor cells and healthy tissue has already been proposed by Nuttens and co-workers.[40] These simulations showed that it was possible to significantly increase the radiation doses when the single radioactive atom coupled to each antibody in classical radioimmunotherapy is replaced by a beta emitting nanoparticle. But the tumor model used for those simulations is valid only for avascular cell clusters, which rarely exceed 0.2 mm diameter.[41–43]

In this paper, we study the doses deposited inside and around a spherical solid tumor when the single radionuclide labeled to antibodies is replaced by a radioactive nanoparticle of 5 nm diam. For that purpose, new three-dimensional vascular models representing the tumor have been developed. For each model, shapes of deposited dose distributions were calculated for the stable oxide molecules $^{90}Y_2O_3$, which are already experimentally produced and well adapted to cure large tumors with nonhomogeneous vasculature. Indeed, the radionuclide yttrium-90 has the advantage of being a pure β emitter with a high energy radiation ($E_{max} \sim 2.3$ MeV) responsible for a long penetration range in tissue ($R_{max} \sim 11$ mm).[44–46]

II. TUMOR MODELS

The MCNPX software is capable of simulating the transport of photons and electrons in matter over a broad energy range. The input file of this code is composed of three types of data, those corresponding to the geometry of the problem (composition, form, and density of the tumor and surrounding healthy tissues), the radioactive sources (nature, emission spectra, and positions inside and near the tumor), and the nature of the desired result (i.e., the deposited energy). Beta spectral data for yttrium-90 were taken from tables on the RADAR site (www.doseinfo-radar.com/RADARDecay.html). The composition and density of malignant and healthy tissues were taken from ICRU Report 44,[47] and three tumor models were considered.

II.A. Avascular model

In our previous work,[40] the solid tumor was represented by a simple sphere of breast tissue surrounded by biological vectors (bVs), and each of them was labeled with one radioactive nanoparticle. We have assumed that the maximum distance between the tumor binding site of the biological vector and the radioactive nanoparticle binding site was around 15 nm.[48–50] Radiolabeled bVs surrounding the tumor were then modeled by a spherical surface that emits radiations. The radius of this surface was chosen 15 nm larger than the tumor radius to comply with the size of antibodies. The same material density was used for diseased and healthy tissues. The dose delivered to the tumor and normal tissues has been evaluated using the pulse-height tally *F8 (MeV/g/nps) offered by MCNPX and converted into Gy.

This model is well adapted as long as the tumor measures hundreds of micrometers in diameter and is not vascularized. However, most larger solid tumors are described by a set of

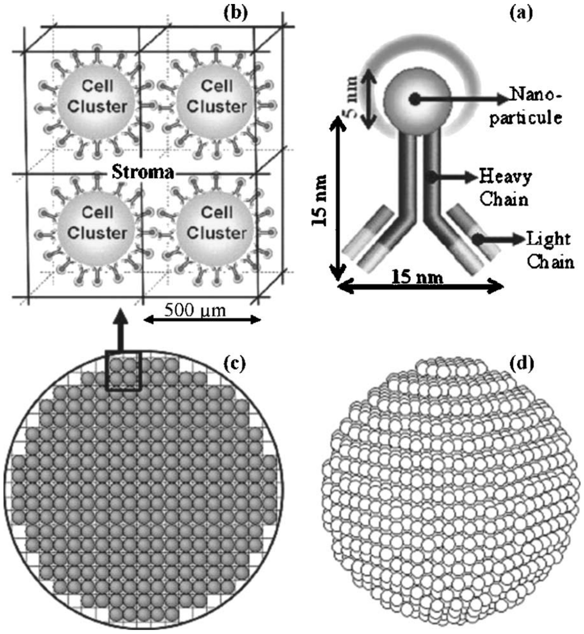

FIG. 1. Uniformly vascularized model: (d) Three-dimensional arrangement of cell units for a tumor radius of 0.5 cm. The sphere contains a total of 3591 cell clusters. (c) Section through the center of the tumor modeled with cell clusters inside a cubic lattice of 500 μm width. (a) Representation of 4 cell units surrounded by antibodies of 15 nm height labeled with a radioactive nanoparticle of 5 nm diameter. The remaining matter inside each cube of the lattice is the stroma. (b) Y-shaped monoclonal antibodies labeled with a radioactive nanoparticle.

cell clusters (also called parenchyma) surrounded by vascularized stroma.[51] In this case, the antibodies can penetrate the tumor, and a radionuclide distribution inside the tumor should be considered.

II.B. Vascular model

For this new model, we hypothesized that the solid tumor is a sphere, and we investigated what happens if the activity is distributed throughout the volume. The idea is to subdivide the tumor sphere into small cubes of 500 μm side length. This size can be decreased or increased according to whether the tumor is poorly or well vascularized. Each site of the cubic lattice is then filled by a spherical cell cluster of 250 μm radius (Fig. 1). The remaining matter inside each cubic lattice represents tumor stroma containing vessels, which could be either a new blood network created through angiogenesis or simply the pre-existing vasculature. The antibodies can penetrate inside the tumor through this vascularization and surround the various cell units. If all cell clusters inside the cubic lattice have the same probability to be reached by an antibody, the distribution of activity is uniform. This set of neoplastic clusters modeling the tumor is at the center of a much larger sphere representing healthy tissue. The matter composition for both healthy and cancerous tissues is identical.

While very simple, this uniformly vascularized model cannot represent large tumors. Indeed, experimental and theoretical studies have also shown that, during angiogenesis, the outer region close to the tumor perimeter is well vascularized by thin capillaries while the center is poorly vascularized by dilated vessels.[52–56] Between these two volumes, the density of blood vessels decreases and their thickness increases. According to the results obtained by Lee *et al.* microvascular density (MVD) at the surface of human malignant melanoma is two times more important than the density observed in healthy tissues (MVD_0) and is continuously decreasing below 50% of MVD_0 at the tumor center.[55] These heterogeneities in blood flow may cause a nonuniform distribution of radioactivity in tumors.[57]

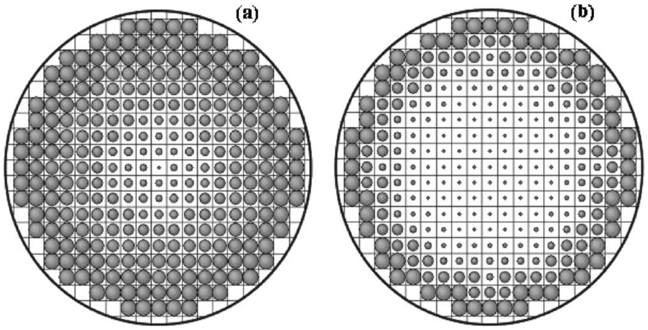

FIG. 2. Schematic arrangement of the nonuniformly vascularized model: Section through the center of a tumor of 0.5 cm radius for (a) linear or (b) exponential radioactive distribution. The size of the cell units depends on the probability to be reached by an antibody.

In order to take this heterogeneity into account, a vascularized model in which a nonuniform distribution of activity inside the tumor has also been developed by subdividing the sphere into concentric shells differing in probabilities to be reached by an antibody. These probabilities have a maximum of 2.0 for cell units localized near the tumor radius and decrease linearly or exponentially toward the center of the tumor volume (Fig. 2) down to a value of 0.2. The drop in probability between 2.0 and 0.2 reproduces the same decrease in MVD observed by Lee and co-workers.[55]

II.C. Necrotic vascular model

When the tumor grows, the organization of the tumor vasculature differs completely from normal tissue. The blood vessels are tortuous and change constantly.[51] Consequently, the center of large tumors is often characterized by a strong decrease of blood vessels causing cellular death and the generation of necrotic areas. This absence of vasculature also represents an important obstacle for the transport of antibodies and drugs. Hence, a more precise estimate of the deposited dose distribution within the tumor volume can be obtained by introducing a central necrotic core that may occupy a significant fraction of the total volume for many tumors.

In this case, the tumor will be described by an inner zone of necrotic cells (or dead cells due to lack of nutrients) and an outer zone of living cells. As in the vascularized models, viable cell clusters and necrotic matter clusters are placed in a three-dimensional regular cubic lattice formed inside the tumor sphere. Figure 3 presents a model of a necrosed tumor of 0.5 cm radius. The side length of the cubic lattice is

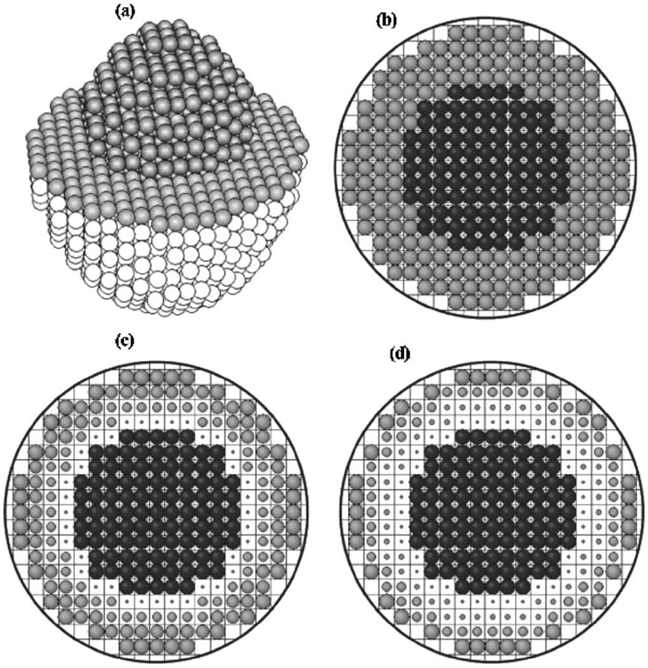

FIG. 3. (a) A cut-away view of a three-dimensional arrangement of cell clusters for a 0.5 cm tumor radius and a 0.32 cm necrotic radius. The maximum number of living cell clusters inside the sphere reaches 2028; (b), (c), and (d) are sections through the center of the tumor modeling for a uniform, linear, and exponential distribution, respectively. The dark region in the center of the tumor corresponds to the area of necrotic cells. The light gray filled circles denote the presence of the viable cell clusters. The size of each cell unit depends on the probability to be reached by an antibody.

500 μm. The two kinds of clusters are differentiated thanks to a necrotic radius below which all the dead matter is combined. The radius of the necrotic core can vary widely with time and tumor type. For this example, we have chosen a radius of about 0.32 cm, meaning that 25% of the total number of cell clusters is nonviable. The same density has been used for the necrotic and living cell clusters, but the access of drugs in the central necrotic core of the tumor is limited. So, the probability to observe a monoclonal antibody around a dead unit is assumed to be zero. Uniform, linear, and exponential decreases take place only in the non-necrotic part of the tumor with a maximum probability of 2.0 in the vicinity of the tumor perimeter and a minimum value of 0.2 around the dead cell units. This model is just an example. The size of the cubic lattice, the radius of the necrotic core, and the probabilities for each cell clusters to be reached by an antibody can vary according to the type of tumor or the characteristics of biological vector. Table I gives the number of viable and nonviable cell clusters for two tumor radii (R_T $=0.5$ and 1.0 cm) and for different necrotic radii (R_N).

II.D. Dose calculation

The use of the tally *F8 (MeV/g/nps) proposed by Nuttens and co-workers[40] to determine the distributions of dose according to the distance from the tumor center is no longer valid for these new vascularized models. Indeed, the tally *F8 calculates the energy deposition in a cell, which is defined by a single density and a simple geometry. The solid tumor, as well as surrounding healthy tissue, in the first model could be subdivided into concentric spherical shells, and each ring represented a cell with a single density. But if the tumor is composed of numerous cell clusters, these same concentric shells will inevitably cross different geometries and densities. Hence, the second and third models require a new method capable of calculating the dose deposited into concentric spherical shells independently of the geometrical problem. The solution was found using the spherical mesh tally (SMESH, type I)[58] that defines virtual spherical grids superimposed on the geometry of the tumor. The deposited dose (MeV/g/nps) evaluated for each mesh of the grid is then converted into Gy.

To determine the total activity A inside the tumor for these new vascularized models, we use the following expression:

$$A = \lambda_{\text{phys}} \times n_u \times n_a \times n_{\text{mAb}},$$

where λ_{phys} corresponds to the radioactive decay constant of the radionuclide. n_u and n_a represent the number of viable tumor cell units (Table I) and the number of radioactive atoms per nanoparticle, respectively. The amount of monoclonal antibody, which surrounds each small cell cluster, denoted n_{mAb}, is obtained by multiplying the surface of a tumor cell unit with the covering fraction. The latter is defined as the number of bound mAb's per unit of surface and hence represents the binding characteristics of the antibody chosen for RIT.

In order to test the deposited dose calculations using the SMESH tally, we have applied this method to the first avascular model for solid tumors of 0.5 and 1.0 cm radius and compared our dose distribution versus radial distance d from

TABLE I. Tumor (R_T) and necrotic (R_N) radii with their associated number of viable cell clusters (# VC) and nonviable cell clusters (# NC). The first column gives the percentage of necrosed units compared with the total number of clusters.

	R_T=0.5 cm			R_T=1.0 cm		
%	R_N	# VC	# NC	R_N	# VC	# NC
0	—	3591	—	—	31071	—
10	0.24	3262	329	0.47	28076	2995
25	0.32	2702	889	0.64	23342	7729
50	0.41	1766	1825	0.80	15370	15701
75	0.46	836	2755	0.92	7358	23713

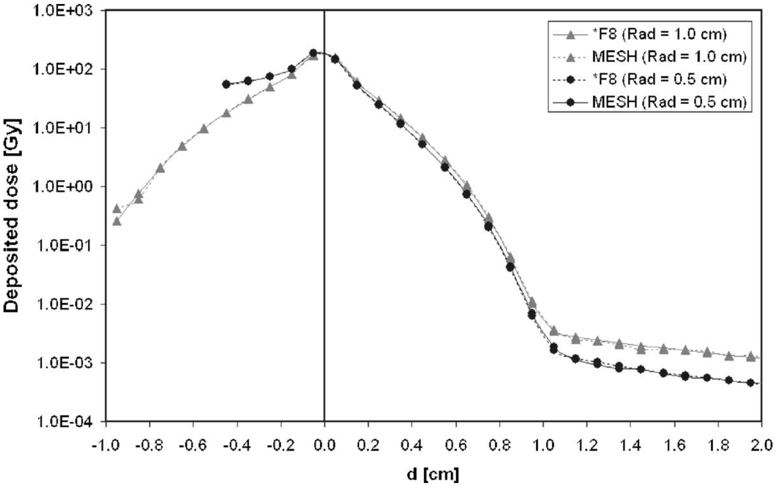

FIG. 4. Deposited dose as a function of distance *d* from the tumor surface for both methods *F8 (dashed line) and spherical MESH tallies (solid line). The comparison is applied to solid tumors of 1.0 cm and 0.5 cm radius surrounded by $^{90}Y_2O_3$ nanoparticles (5 nm diameter). The values for biological half time (three days) and the covering fraction (8.92×10^8 mAb/cm^2) are identical to those chosen by Nuttens *et al.* (Ref. 40).

the tumor surface with the previous results obtained by Nuttens and co-workers (Fig. 4). The minimal thickness between two distances *d* is 1 mm in order to satisfy the requirement of MCNPX for electron dosimetry.[59,60] The shape of the dose distributions is very similar, which demonstrates the validity of the spherical SMESH tally for calculating the deposited energy inside the tumor.

III. RESULTS AND DISCUSSION

The various geometrical models presented in the previous section have been introduced in the MCNPX 2.5.0 code to analyze the deposited dose inside and around cancer cells as a function of distance from the center for two tumor radii (0.5 and 1.0 cm). In these simulations, the tumors are irradiated by 5 nm diameter nanoparticles of $^{90}Y_2O_3$. Such nanoclusters can contain about 1.73×10^3 atoms of yttrium-90 but, due to the short physical halflife of this radioelement (T_{phys}=2.67 days), we consider that only 60% are still radioactive when the antibody reaches the tumor. Indeed, biodistribution data and imaging studies have shown that two days are needed to obtain the maximum accumulation of the radiolabeled antibodies within the tumor after intravenous administration.[61–64] This percentage of radioactive atoms could increase by applying the bispecific monoclonal antibody (bsMAb) pretargeting approach. In this case, the radioisotopes are injected one to two days after the bsMAb have penetrated the tumor.[2,65] Hence, the delay time between the antibodies injection and the binding with antigen have an influence on our simulations. The clearance of the radiolabeled antibodies is also taken into account by incorporating a biological halflife of three days in our calculations.[66]

Three geometric factors can influence the results of these dose distributions. First, we assume that all tumors have a spherical geometry, but the radius sizes and the inner lattice dimensions can be adjusted to work with larger tumors or smaller cell clusters to improve the precision of the method. The restriction of analyses to a cubic lattice of 500 μm length is simply a question of simulation time and computational convenience. Second, the radioactivity distribution throughout the tumor volume can be uniform, linear, or exponential. These distributions are obtained by tuning the probability for an antibody to reach a cell cluster localized in a specific depth inside the sphere. It allows us to take into consideration the tumor vasculature. The third geometrical factor is the volume of the necrotic core. In this zone, the probability of finding a radioactive nanocluster around a cell unit is simply null and only radiation coming from nonnecrotic cell clusters can act on the tumor.

The covering fraction, defined as the number of bound mAb's per unit of tumor surface, is adjusted to insure a minimal dose of 50 Gy everywhere inside the solid tumor.[67] For the avascular model, this minimum is reached at the center of a 0.5 cm radius sphere if the covering fraction corresponds to 7.42×10^8 mAb/cm^2. With such a value, the total activity delivered to the tumor is equivalent to 7 MBq. For a larger tumor, the penetration depth of beta particles emitted from ^{90}Y is not sufficient to provide enough activity within the central part. Using the same value of covering fraction for the 1.0 cm radius tumor, the total activity increases to 29 MBq. For the vascularized models, with or without necrosis, the weaker values of deposited dose are rather observed at the surface of the sphere. The covering fractions obtained for both solid tumors of 0.5 and 1.0 cm radius are 5.94×10^7 and 4.46×10^7 mAb/cm^2, respectively. These values can be used in our simulations because they remain inferior to the typical values of covering fractions, which range from 10^8 to 10^{10} mAb/cm^2.[45] The total activity *A* inside the tumor for these two new values of covering fraction is 5 MBq (R_T=0.5 cm) and 34 MBq (R_T=1.0 cm). Table II presents the maximum doses delivered inside the tumor and doses deposited at the center, at the surface, and 1 mm away in healthy tissue for vascular and the different avascular models.

The first MCNPX simulations for the three different antibody distributions of radionuclide have been performed without a necrotic core and compared with the results of the previous avascular model. Figures 5(a) and 5(b) illustrate, respectively, dose distributions in tumors of radii 0.5 and 1.0 cm for $^{90}Y_2O_3$ distributed uniformly, linearly, exponentially, or coming only from the surface.

TABLE II. Maximal doses absorbed by the tumor (Max) and doses at the center (Cent), at the surface (Surf) or at 1 mm beyond the surface (Out) resulting from simulations for $^{90}Y_2O_3$ distributed uniformly, linearly, exponentially or around the surface of the tumor sphere. For each radius, the first column gives the doses if the tumor has no necrotic matter. The three other columns present results when 10, 25, or 50% of the cell units are necrosed.

		Tumor of 0.5 cm radius				Tumor of 1.0 cm radius			
		No Necrosed	10% Necrosed	25% Necrosed	50% Necrosed	No Necrosed	10% Necrosed	25% Necrosed	50% Necrosed
Surface	Cent	53				0			
	Max	192				174			
	Surf	150				164			
	Out	54				61			
Uniform	Cent	270	140	101	72	229	45	14	4
	Max	270	144	208	180	229	132	231	251
	Surf	52	55	59	66	52	57	67	85
	Out	23	24	26	29	24	26	31	40
Linear	Cent	175	101	80	68	103	21	6	2
	Max	204	161	173	183	204	168	226	227
	Surf	56	61	64	69	60	73	80	95
	Out	25	27	28	30	28	34	37	44
Exponential	Cent	110	92	74	65	754	15	4	1
	Max	169	166	176	183	207	186	207	243
	Surf	64	64	67	70	90	80	97	105
	Out	28	28	29	30	41	37	45	48

III.A. Doses in the tumor center and in healthy tissues

The goal in radioimmunotherapy is to deposit high enough doses to the tumor while minimizing the radiation of healthy tissue. The results presented in Fig. 5 indicate that the radioactivity distribution has a considerable impact on the doses delivered at the center if the tumor had no necrosis. Indeed, the central doses for a tumor of 0.5 cm radius range from 270 Gy for the uniform activity to 110 Gy when the decrease of radionuclides is exponential, which represents a difference of about 160 Gy between both values. A similar decrease is observed for the tumors of 1.0 cm radius where the central doses for the uniform, linear, and exponential radionuclide distributions are, respectively, 230, 100, and 75 Gy. Either for small or large tumors, the values of the deposited doses in the central region are very different according to the type of activity distribution. All these dose values are, however, larger than 50 Gy, which is the value obtained for an avascular tumor of 0.5 cm radius.

Inversely, radionuclide distributions seem to have only a low influence on the doses deposited on the tumor surface or in the surrounding normal tissue. Moreover, doses delivered by the radioactive nanoparticles remain very weak in healthy tissue compared to those absorbed by the malignancy. Simulations show that doses lower than 30 Gy are obtained 1 mm beyond the tumoral surface for the vascular model. These values of deposited doses around the surface increase drastically if we want to obtain a minimum of 50 Gy at the center of an avascular tumor for which there is no penetration of the radiolabeled antibodies. Hence, these last results show that, even if the vasculature inside the tumor is totally heterogeneous, the survival of healthy cells is ensured by the penetrability of the radiolabeled antibodies.

III.B. Maximal doses

The two graphs of Fig. 5 show that the maximal doses are deposited inside the tumor independently of the radioactivity distribution. When the distribution is uniform, the highest deposited dose is reached at the center for small tumors [Fig. 5(a)] or presents a central plateau for larger tumors [Fig. 5(b)] before decreasing in the vicinity of normal tissue. For linear or exponential distributions, the maximal doses are delivered close to the surface but with a deeper radial position within the tumor when the distribution of the radiolabeled antibodies decreases linearly.

The maximum deposited dose decreases from uniform to linear and to an exponential activity distribution within a small tumor [Fig. 5(a)]. In a larger tumor [Fig. 5(b)], smaller differences are observed. However, simulations show that different parts of this larger tumor can be differently targeted according to the type of activity distribution. When the distribution of radionuclide decreases exponentially, it is in particular the diseased cells near the surface that receive the highest radiation doses. But, when a homogeneous vasculature is modeled, the tumor cells at the center are strongly irradiated compared to those located near the surface. If the aim is to kill the cancer cells within the center of the tumor, 50 Gy is more easily obtained in the case of a uniform activity distribution. On the other hand, to target the cells at the tumor periphery, larger deposited doses are obtained in the case of an exponential distribution.

III.C. Necrotic core

The influence of a necrotic core on the deposited doses can be analyzed by introducing different necrotic volumes in the vascular model. Figures 6–11 illustrate the deposited

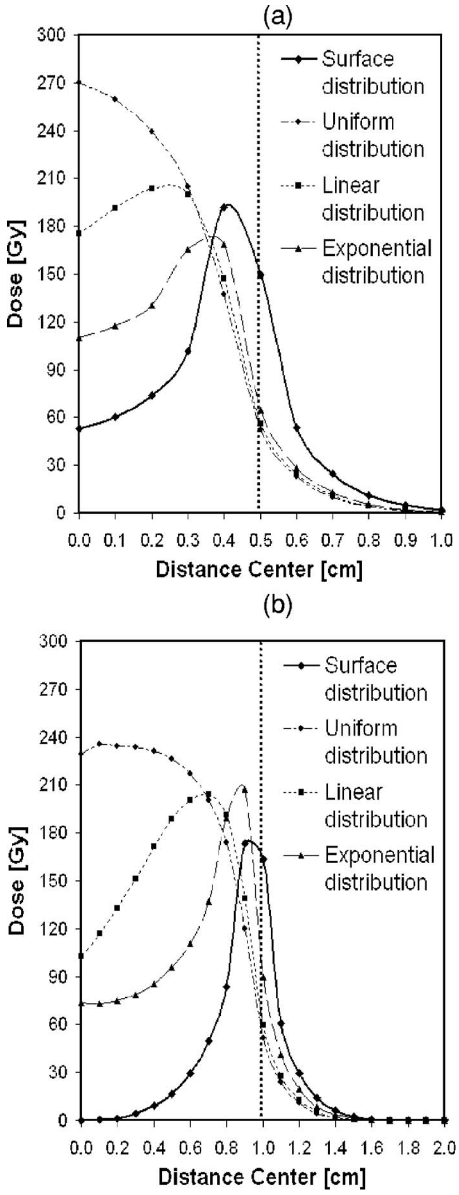

FIG. 5. Comparison of deposited dose profiles for $^{90}Y_2O_3$, in Gy, as a function of the distance from center for both tumor radii of (a) 0.5 and (b) 1.0 cm. The width of the cubic lattice is 500 μm.

dose profiles for tumors of 0.5 and 1.0 cm radii when 10% (Figs. 6 and 9), 25% (Figs. 7 and 10), and 50% (Figs. 8 and 11) of cell units are not alive. For each necrotic core size, uniform, linear, and exponential distributions of radionuclide have been applied only on the viable cell clusters. The deposited dose profiles are calculated with the same total activity as the non-necrotic vascular model, i.e., 5 MBq (R_T =0.5 cm) and 34 MBq (R_T=0.5 cm).

By comparing Fig. 6 with Figs. 7 and 8 or Fig. 9 with Figs. 10 and 11, we see that the deposited dose curves for the three radionuclide distributions (uniform, linear, and exponential) are increasingly superimposed when the necrotic volume increases. However, the shapes of these curves remain very different from those obtained with the avascular model for which smaller doses are deposited inside the tumor. Conversely, the surrounding healthy tissue receives more irradiation coming from the radiolabeled antibodies located at the surface in this avascular model. Moreover, the deposited doses are lower in healthy tissue when the radius of the necrotic core decreases.

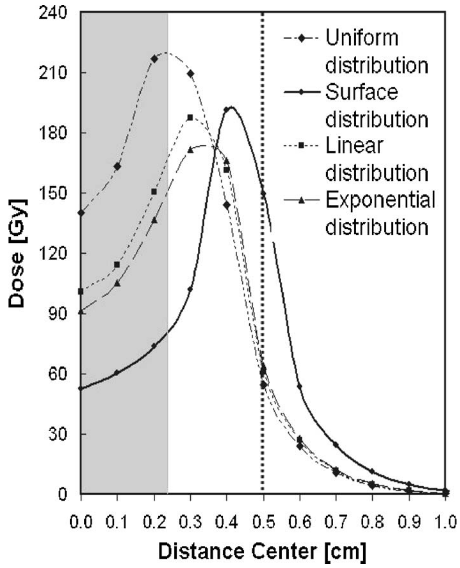

FIG. 6. Deposited dose distributions for $^{90}Y_2O_3$, in Gy, as a function of radial distance from the center for a vascularized tumor of 0.5 cm radius. The radial dependence of deposited doses is simulated for uniform, linear, and exponential distributions of antibody in the tumor. The radius of the necrosed core (R_N) is 0.24 cm, meaning that 10% of the total number of cell clusters is nonviable.

When the percentage of necrosed units increases, central deposited doses decrease due to the limited range of electrons in the matter. For tumors of 1.0 cm radius, these values

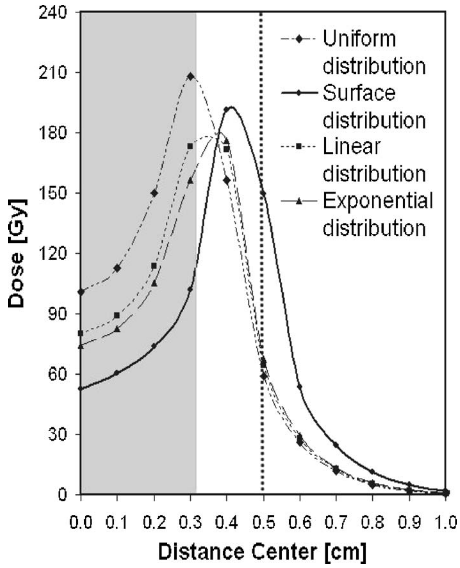

FIG. 7. Deposited dose distributions for $^{90}Y_2O_3$, in Gy, as a function of radial distance from the center for a vascularized tumor of 0.5 cm radius. The radial dependence of deposited doses is simulated for uniform, linear, and exponential distributions of antibody in the tumor. The radius of the necrosed core (R_N) is 0.32 cm, meaning that 25% of the total number of cell clusters is nonviable.

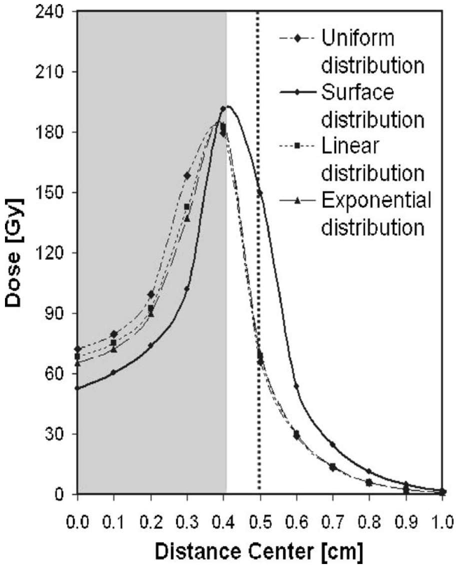

FIG. 8. Deposited dose distributions for $^{90}Y_2O_3$, in Gy, as a function of radial distance from the center for a vascularized tumor of 0.5 cm radius. The radial dependence of deposited doses is simulated for uniform, linear, and exponential distributions of antibody in the tumor. The radius of the necrosed core (R_N) is 0.41 cm, meaning that half of the total number of cell clusters is nonviable.

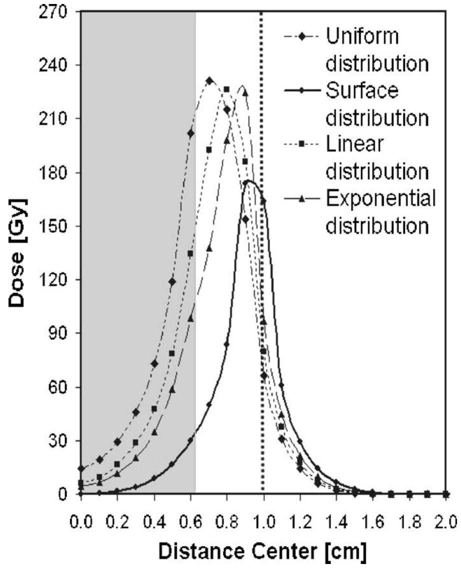

FIG. 10. Deposited dose distributions for $^{90}Y_2O_3$, in Gy, as a function of radial distance from the center for a vascularized tumor of 1.0 cm radius. The radial dependence of deposited doses is simulated for uniform, linear, and exponential distributions of antibody in the tumor. The radius of the necrosed core (R_N) is 0.64 cm, meaning that 25% of the total number of cell clusters is nonviable.

are even lower than 50 Gy. However, all the cells located in the necrotic part of the tumor are already dead and do not require irradiation. In this case, minimum values of 50 Gy must be obtained only around the necrotic core in order to have good therapeutic effects. If we look at results from Fig. 9, the deposited doses calculated near the necrotic tissue are 216, 202, and 108 Gy for the three different activity distributions. These numbers increase similarly when the percentage of necrotic tissue is more important. All doses are clearly sufficient to kill the cells around the necrotic core. Consequently, the presence of nonviable cell clusters and heterogeneities in the vasculature does not appear to be an obstacle to delivering doses significant enough to destroy the solid tumor.

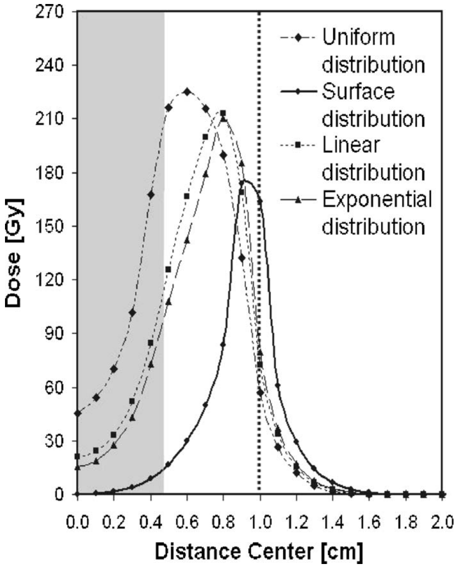

FIG. 9. Deposited dose distributions for $^{90}Y_2O_3$, in Gy, as a function of radial distance from the center for a vascularized tumor of 1.0 cm radius. The radial dependence of deposited doses is simulated for uniform, linear, and exponential distributions of antibody in the tumor. The radius of the necrosed core (R_N) is 0.47 cm, meaning that 10% of the total number of cell clusters is nonviable.

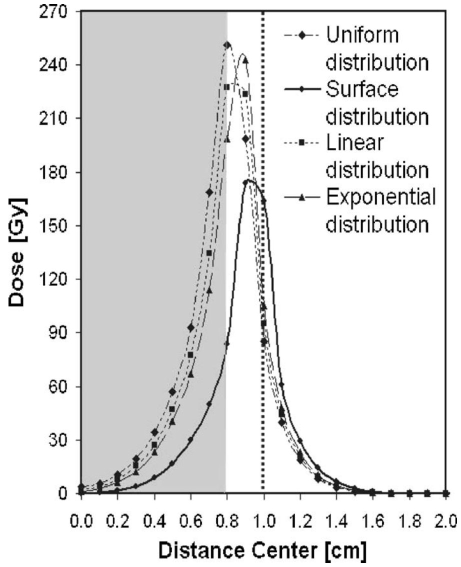

FIG. 11. Deposited dose distributions for $^{90}Y_2O_3$, in Gy, as a function of radial distance from the center for a vascularized tumor of 1.0 cm radius. The radial dependence of deposited doses is simulated for uniform, linear, and exponential distributions of antibody in the tumor. The radius of the necrosed core (R_N) is 0.80 cm, meaning that half of the total number of cell clusters is nonviable.

IV. CONCLUSION

MCNPX can be used in radioimmunotherapy to evaluate the energy deposition in tumor nodules and determine the most appropriate therapeutic treatment for a patient. However, this software requires accurate information on the structure and the microscopic distribution of radioactivity coming from the radiolabeled antibodies. In this work, the vascularized tumor was modeled by a set of spherical cell clusters of 500 μm diameter arranged in a simple cubic lattice structure. Three different antibody distributions have been tested in the simulations: Uniform, linear, and exponential. We have also introduced the possibility to have a central necrotic core inside the tumor where the probability to observe an antibody is supposed to be null. The shapes of spatial dose distributions are strongly influenced by the morphology and the size of the solid tumors, indicating the importance of choosing the optimal geometries to represent the tumor.

Spatial deposited dose distributions confirm the benefit of using radiolabeled nanoparticles containing hundreds of radioactive atoms rather than antibodies coupled to a single radionuclide to treat solid and poorly vascularized tumors in RIT. Indeed, even if the antibodies are distributed exponentially, doses higher than 50 Gy are delivered in the entire tumor. The use of radioactive nanoparticles thus limits the problems of antibody penetrability often observed in classical RIT when a single radioactive atom is labeled to each specific antibody.

ACKNOWLEDGMENTS

This research (Targan Project) is supported by the Walloon Region (Belgium). C.M. and O.F. are senior research associates of FNRS (Fonds National de la Recherche Scientifique, Belgium).

[a] Author to whom correspondence should be addressed. Telephone: 0032-81-725479; Fax: 0032-81-725474. Electronic mail: bouchat@fundp.ac.be

[1] D. M. Goldenberg, "Targeted therapy of cancer with radiolabeled antibodies," J. Nucl. Med. **43**, 693–713 (2002).

[2] D. M. Goldenberg and R. M. Sharkey, "Advances in cancer therapy with radiolabeled monoclonal antibodies," Q. J. Nucl. Med. Mol. Imaging **50**, 248–264 (2006).

[3] T. A. Waldmann, "Immunotherapy: Past, present and future," Nat. Med. **9**, 269–277 (2003).

[4] P. Carmeliet, "Angiogenesis in health and disease," Nat. Med. **9**, 653–660 (2003).

[5] J. Folkman, "Angiogenesis in cancer, vascular, rheumatoid and other disease," Nat. Med. **1**, 27–31 (1995).

[6] J. Ahlskog, G. Paganelli, and D. Neri, "Vascular tumor targeting," Q. J. Nucl. Med. Mol. Imaging **50**, 296–309 (2006).

[7] A. Gruaz-Guyon, O. Raguin, and J. Barbet, "Recent advances in pretargeted radio-immunotherapy," Curr. Med. Chem. **12**, 319–338 (2005).

[8] E. J. Postema, O. C. Boerman, W. J. Oyen, J. M. Raemaekers, and F. H. Corstens, "Radioimmunotherapy of B-cell non-Hodgkin's lymphoma," Eur. J. Nucl. Med. **28**, 1725–1735 (2001).

[9] T. E. Witzig, "Radioimmunotherapy for patients with relapsed B-cell non-Hodgkin lymphoma," Cancer Chemother. Pharmacol. **48**, 91S-95S (2001).

[10] C. A. White, J. R. Berlfein, and A. J. Grillo-Lopez, "Antibody-targeted immunotherapy for treatment of non-Hodgkin's lymphoma," Curr. Pharm. Biotechnol. **1**, 303–312 (2000).

[11] D. M. Goldenberg, "The role of radiolabeled antibodies in the treatment of non-Hodgkin's lymphoma: the coming of age of radioimmunotherapy," Crit. Rev. Oncol. Hematol. **39**, 195–201 (2001).

[12] G. A. Wiseman, C. A. White, R. B. Sparks, W. D. Erwin, D. A. Podoloff, D. Lamonica, N. L. Bartlett, J. Anthony Parker, W. L. Dunn, S. M. Spies, R. Belanger, T. E. Witzig, and B. R. Leigh, "Biodistribution and dosimetry results from a phase III prospectively randomized controlled trial of Zevalin radioimmunotherapy for low-grade, follicular, or transformed B-cell non-Hodgkin's lymphoma," Crit. Rev. Oncol. Hematol. **39**, 181–194 (2001).

[13] W. A. Bethge and B. M. Sandmaier, "Targeted cancer therapy using radiolabeled monoclonal antibodies," Technol. Cancer Res. Treat. **4**, 393–405 (2005).

[14] S. V. Govindan, G. L. Griffiths, H. J. Hansen, I. D. Horak, and D. M. Goldenberg, "Cancer therapy with radiolabeled and drug/toxin-conjugated antibodies," Technol. Cancer Res. Treat. **4**, 375–391 (2005).

[15] R. M. Sharkey and D. M. Goldenberg, "Perspectives on cancer therapy with radiolabeled monoclonal antibodies," J. Nuc. Med. Treat. **46**, 115S-127S (2005).

[16] D. M. Goldenberg, "Advancing role of radiolabeled antibodies in the therapy of cancer," Cancer Immunol. Immunother **52**, 281–296 (2003).

[17] D. L. Peng, T. Hihara, and K. Sumiyama, "Structure and magnetic properties of FePt alloy cluster-assembled film," J. Magn. Magn. Mater. **277**, 201–208 (2004).

[18] A. L. Thomann, J. P. Salvetat, Y. Breton, C. Andreazza-Vignolle, and P. Brault, "Thermal stability of metal nanoclusters formed by low-pressure plasma sputtering," Thin Solid Films **428**, 242–247 (2003).

[19] A. Naudon, D. Babonneau, D. Thiaudière, and S. Lequien, "Grazing-incidence small-angle x-ray scattering applied to the characterization of aggregates in surface regions," Physica B **283**, 69–74 (2000).

[20] Y. Saito, "Nanoparticles and filled nanocapsules," Carbon **33**, 979–988 (1995).

[21] S. M. Moghimi, A. C. Hunter, and J. C. Murray, "Long-circulating and target-specific nanoparticles: Theory to practice," Pharmacol. Rev. **53**, 283–318 (2001).

[22] S. M. Moghimi and J. Szebeni, "Stealth liposomes and long circulating nanoparticles: Critical issues in pharmacokinetics, opsonization, and protein-binding properties," Prog. Lipid Res. **42**, 463–478 (2003).

[23] S. M. Moghimi and A. C. Hunter, "Recognition by macrophages and liver cells of opsonized phospholipid vesicles and phospholipid headgroups," Pharm. Res. **18**, 1–8 (2001).

[24] E. D. Owens, III and N. A. Peppas, "Opsonization, biodistribution, and pharmacokinetics of polymeric nanoparticles," Int. J. Pharm. **307**, 93–102 (2006).

[25] S. M. Moghimi, A. C. Hunter, and J. C. Murray, "Nanomedicine: Current status and future prospect," FASEB J. **19**, 311–330 (2005).

[26] R. Gref, M. Luck, P. Quellec, M. Marchand, E. Dellacherie, S. Harnish, T. Blunk, and R. H. Muller, "Stealth corona-core nanoparticles surface modified by polyethylene glycol (PEG): influences of the corona (PEG chain length and surface density) and of the core composition on phagocytic uptake and plasma protein adsorption," Colloids Surf., B **18**, 301–313 (2000).

[27] Y. Yi, J. H. Kim, H.-W. Kang, H. S. Oh, S. W. Kim, and M. H. Seo, "A polymeric nanoparticle consisting of mPEG-PLA-Toco and PLMA-COONa as a drug carrier: improvements in cellular uptake and biodistribution," Pharm. Res. **22**, 200–208 (2005).

[28] C. C. Berry and A. S. G. Curtis, "Functionalisation of magnetic nanoparticles for applications in biomedicine," J. Leukoc Biol. **78**, 585–594 (2005).

[29] S. E. McNeil, "Nanotechnology for the biologist," J. Leukoc Biol. **78**, 585–594 (2005).

[30] M. Yokoyama, "Drug targeting with nano-sized carrier systems," J. Artif. Organs **8**, 77–84 (2005).

[31] W. J. Parak, T. Pellegrino, and C. Plank, "Labelling of cells with quantum dots," Nanotechnology **16**, R9–R25 (2005).

[32] X. Wu, H. Liu, K. N. Haley, J. A. Treadway, J. P. Larson, N. Ge, F. Peale, and M. P. Bruchez, "Immunofluorescent labeling of cancer marker Her2 and other cellular targets with semiconductor quantum dots," Nat. Biotechnol. **21**, 41–46 (2003).

[33] X. Gao, Y. Cui, R. M. Levenson, L. W. K. Chung, and S. Nie, "*In vivo* cancer targeting and imaging with semiconductor quantum dots," Nat. Biotechnol. **22**, 969–976 (2004).

[34] M. N. Rhyner, A. M. Smith, X. Gao, H. Mao, L. Yang, and S. Nie, "Quantum dots and multifunctional nanoparticles: new contrast agents for tumor imaging," Nanomedicine **1**, 209–217 (2006).

[35] J. T. Kemshead and J. Ugelstad, "Magnetic separation techniques: their application to medicine," Mol. Cell. Biochem. **67**, 11–18 (1985).

[36] V. Choesmel, P. Anract, H. Hoifodt, J. P. Thiery, and N. Blin, "A relevant immunomagnetic assay to detect and characterize epithelial cell adhesion molecule-positive cells in bone marrow from patients with breast carcinoma: immunomagnetic purification of micrometastases," Cancer **101**, 693–703 (2004).

[37] C. Loo, A. Lowery, N. Halas, J. West, and R. Drezek, "Immunotargeted nanoshells for integrated cancer imaging and therapy," Nano Lett. **5**, 709–711 (2005).

[38] L. R. Hirsch, R. J. Stafford, J. A. Bankson, S. R. Sershen, B. Rivera, R. E. Price, J. D. Hazle, N. J. Halas, and J. L. West, "Nanoshell-mediated near-infrared thermal therapy of tumors under magnetic resonance guidance," Proc. Natl. Acad. Sci. U.S.A. **100**, 13549–13554 (2003).

[39] G. Wang, T. Huang, R. W. Murray, L. Menard, and R. G. Nuzzo, "Near-IR luminescence of monolayer-protected metal clusters," J. Am. Chem. Soc. **127**, 812–813 (2005).

[40] V. E. Nuttens, A.-C. Wera, V. Bouchat, and S. Lucas, "Determination of biological vector characteristics and nanoparticle dimensions for radioimmunotherapy with radioactive nanoparticles," Appl. Radiat. Isot. (accepted).

[41] D. Ribatti, A. Vacca, and F. Dammacco, "The role of vascular phase in solid tumor growth: A historical review," Neoplasia **1**, 293–302 (1999).

[42] J. Folkman, E. Merler, C. Abernathy, and G. Williams, "Isolation of a tumor factor responsible or angiogenesis," J. Exp. Med. **133**, 275–288 (1971).

[43] R. M. Sutherland, "Cell and environment interactions in tumor microregions: The multicell spheroid model," Science **240**, 177–184 (1988).

[44] M. Cremonesi, M. Ferrari, L. Bodei, G. Tosi, and G. Paganelli, "Systemic and locoregional dosimetry in receptor radionuclide therapy with peptides," Q. J. Nucl. Med. Mol. Imaging **50**, 288–295 (2006).

[45] R. W. Howell, D. V. Rao, and K. S. R. Sastry, "Macroscopic dosimetry for radioimmuno-therapy: Nonuniform activity distributions in solid tumors," Med. Phys. **16**, 66–74 (1989).

[46] E. B. Van Dieren, M. A. B. D. Plaizier, A. Van Lingen, J. C. Roos, G. W. Barendsen, and G. J. J. Teule, "Absorbed dose distribution of the auger emitters 67Ga and 125I and the β-emitters 67Cu, 90Y, 131I, and 186Re as a function of tumor size, uptake, and intracellular distributin," Int. J. Radiat. Oncol., Biol., Phys. **36**, 197–204 (1996).

[47] ICRU Report 44, "Tissue substitutes in radiation dosimetry and measurement," (International Commission on Radiation Units and Measurements, Bethesda, MD, 1989), p 22.

[48] S. Lin, C.-K. Lee, Y.-H. Lin, S.-Y. Lee, B.-C. Sheu, J.-C. Tsai, and S.-M. Hsu, "Homopolyvalent antibody-antigen interaction kinetic studies with use of a dual-polarization interferometric biosensor," Biosens. Bioelectron. **22**, 715–721 (2006).

[49] A. S. Paulo and R. Garcia, "High-resolution imaging of antibodies by tapping-mode atomic force microscopy: attractive and repulsive tip-sample interaction regimes," Biophys. J. **78**, 1599–1605 (2006).

[50] L. Cser, I. A. Gladkib, F. Franek, and Yu. M. Ostanevich, "Investigation of antibody structures by scattering techniques," Colloid Polym. Sci. **259**, 625–640 (1981).

[51] H. F. Dvorak, J. A. Nagy, and A. M. Dvorak, "Structure of solid tumors and their vasculature: Implications for therapy with monoclonal antibodies," Cancer Cells **3**, 77–85 (1991).

[52] B. Döme, S. Paku, B. Somlai, and J. Timar, "Vascularization of cutaneous melanoma involves vessel co-option and has clinical significance," J. Pathol. **197**, 355–362 (2002).

[53] J. A. M. Beliën, P. J. van Diest, and J. P. A. Baak, "Relation between vascularization and proliferation in invasive breast cancer," J. Pathol. **189**, 309–318 (1999).

[54] C. Schlueter, H. Weber, B. Meyer, P. Rogalla, K. Röser, S. Hauke, and J. Bullerdiek, "Angiogenic signaling through hypoxia," Am. J. Pathol. **166**, 1259–1263 (2005).

[55] D.-S. Lee, H. Rieger, and K. Bartha, "Flow correlated percolation during vascular remodeling in growing tumors," Phys. Rev. Lett. **96**, 058104 (2006).

[56] K. Bartha and H. Rieger, "Vascular network remodeling via vessel cooption, regression and growth in tumors," J. Theor. Biol. **241**, 903–918 (2006).

[57] J. L. Humm and L. M. Cobb, "Nonuniformity of tumor dose in radioimmunotherapy," J. Nucl. Med. **31**, 75–83 (1990).

[58] D. B. Pelowitz, ed., "MCNPX User's Manual, Version 2.5.0," LA-CP-05-0369 (2005).

[59] N. Reynaert, H. Palmans, H. Thierens, and R. Jeraj, "Parameter dependence of the MCNP electron transport in determining dose distributions," Med. Phys. **29**, 2446–2454 (2002).

[60] D. R. Schaart, J. Th.M. Jansen, J. Zoetelief, and P. F. A. de Leege, "A comparison of MCNP4C electron transport with ITS 3.0 and experiment at incident energies between 100 keV and 20 MeV: influence of voxel size, substeps and energy indexing algorithm," Phys. Med. Biol. **47**, 1459–1484 (2002).

[61] P. Karnami and K. Kairemo, "Targeting endothelial growth with monoclonal antibodies against Tie-1 kinase in mouse models," Clin. Cancer Res. **9**, 3821s–3826s (2003).

[62] A. Jekunen, K. Kairemo, and P. Karnami, "*In vivo* modulators of antibody kinetics," Acta Oncol. **35**, 267–271 (1996).

[63] S. Palm, R. M. Enmon, Jr., C. Matei, K. S. Kolbert, S. Xu, P. B. Zanzonico, R. L. Finn, J. A. Koutcher, S. M. Larson, and G. Sgouros, "Pharmacokinetics and biodistribution of ^{86}Y-Trastuzumab for ^{90}Y dosimetry in an ovarian carcinoma model: correlative MicroPET and MRI," J. Nucl. Med. **44**, 1148–1155 (2003).

[64] F. T. Lee, A. Rigopoulos, C. Hall, K. Clarke, S. H. Cody, F. E. Smyth, Z. Liu, M. W. Brechbiel, N. Hanai, E. C. Nice, B. Catimel, A. W. Burgess, S. Welt, G. Ritter, L. J. Old, and A. M. Scott, "Specific localization, gamma camera imaging, and intracellular trafficking of radiolabeled chimeric anti-G_{D3} ganglioside monoclonal antibody KM871 in SK-MEL-28 melanoma xenografts," Cancer Res. **61**, 4474–4482 (2001).

[65] C.-H. Chang, R. M. Sharkey, E. A. Rossi, H. Karacay, W. McBride, H. J. Hansen, J.-F. Chatal, J. Barbet, and D. M. Goldenberg, "Molecular advances in pretargeting radioimunotherapy with bispecific antibodies," Mol. Cancer Ther. **1**, 553–563 (2002).

[66] K. Tobinai, Y. Kobayashi, and M. Narabayashi, "Feasibility and pharmacokinetic study of a chimeric anti-CD20 monoclonal antibody (IDEC-C2B8, rituximab) in relapsed B-cell lymphoma," Ann. Oncol. **9**, 527–534 (1998).

[67] D. M. Goldenberg, David M. Goldenberg, R. M. Sharkey, G. Paganelli, J. Barbet, and J.-F. Chatal, "Antibody pretargeting advances cancer radioimmunodetection and radioimmunotherapy," J. Clin. Oncol. **24**, 823–834 (2006).